

## RESEARCH ARTICLE

## Nuclear position modulates long-range chromatin interactions

Elizabeth H. Finn<sup>1\*</sup>, Tom Misteli<sup>2\*</sup>

**1** Program in Cell Cycle and Cancer Biology, Oklahoma Medical Research Foundation, Oklahoma City, Oklahoma, United States of America, **2** National Cancer Institute, National Institutes of Health, Bethesda, Maryland, United States of America

\* [elizabeth-finn@omrf.org](mailto:elizabeth-finn@omrf.org) (EHF); [tom.misteli@nih.gov](mailto:tom.misteli@nih.gov) (TM)

**OPEN ACCESS**

**Citation:** Finn EH, Misteli T (2022) Nuclear position modulates long-range chromatin interactions. *PLoS Genet* 18(10): e1010451. <https://doi.org/10.1371/journal.pgen.1010451>

**Editor:** Bas van Steensel, Netherlands Cancer Institute, NETHERLANDS

**Received:** July 4, 2022

**Accepted:** September 28, 2022

**Published:** October 7, 2022

**Copyright:** This is an open access article, free of all copyright, and may be freely reproduced, distributed, transmitted, modified, built upon, or otherwise used by anyone for any lawful purpose. The work is made available under the [Creative Commons CC0](https://creativecommons.org/licenses/by/4.0/) public domain dedication.

**Data Availability Statement:** All spot positions generated and used can be found at: [10.6084/m9.figshare.20205875](https://doi.org/10.6084/m9.figshare.20205875) The python pipeline used for image analysis can be found at: <https://github.com/elfinn/cell-and-spot-segmentation> The R script used to calculate distances and generate figures can be found at: <https://github.com/elfinn/radpos-r-code>.

**Funding:** Both TM and EHF were supported by the Intramural Program of the NIH, the NCI Center for Cancer Research (1 ZIA BC010309-23). The funders had no role in study design, data collection

## Abstract

The human genome is non-randomly organized within the cell nucleus. Spatial mapping of genome folding by biochemical methods and imaging has revealed extensive variation in locus interaction frequencies between cells in a population and between homologs within an individual cell. Commonly used mapping approaches typically examine either the relative position of genomic sites to each other or the position of individual loci relative to nuclear landmarks. Whether the frequency of specific chromatin-chromatin interactions is affected by where in the nuclear space a locus is located is unknown. Here, we have simultaneously mapped at the single cell level the interaction frequencies and radial position of more than a hundred locus pairs using high-throughput imaging to ask whether the location within the nucleus affects interaction frequency. We find strong enrichment of many interactions at specific radial positions. Position-dependency of interactions was cell-type specific, correlated with local chromatin type, and cell-type-specific enriched associations were marked by increased variability, sometimes without a significant decrease in mean spatial distance. These observations demonstrate that the folding of the chromatin fiber, which brings genomically distant loci into proximity, and the position of that chromatin fiber relative to nuclear landmarks, are closely linked.

## Author summary

A gene's nuclear environment is defined by its distance to other genes as well as its distance to nuclear structures such as the nuclear periphery. While both of these features have been shown to be important for gene function, they are typically studied separately. We performed the first systematic analysis comparing these two features. We determined that at the level of single chromosomes the frequency of interaction of loci is related to their location in the cell nucleus, suggesting that genome organization relative to itself and relative to nuclear landmarks are closely interwoven.

and analysis, decision to publish, or preparation of the manuscript.

**Competing interests:** The authors have declared that no competing interests exist.

## Introduction

The mammalian genome within the cell's nucleus is non-randomly organized [1]. The spatial organization of the genome is guided by two general principles. The first is chromatin folding, which refers to the position of a genomic locus relative to other loci mediated by the interaction of the chromatin fiber over short and long genomic distances. The second is nuclear organization, which refers to the 3D position of a genomic locus relative to nuclear bodies, for example the nuclear lamina or nuclear speckles [1–4].

Chromatin folding is largely thought to arise via the combined effect of two molecular processes: loop extrusion and heterochromatin self-association [5,6]. Sequence-specific chromatin loops are generated by loop extrusion, in which the cohesin motor protein complex spools the chromatin fiber through its ring until it meets the boundary protein CTCF, and the cohesin complex stalls and stabilizes associations between two distal CTCF sites in the form of a loop [7–10]. While any given cohesin complex likely only binds for a short time [7], consistent binding of multiple complexes and regular extrusion of loops in the region between two convergent CTCF sites ultimately creates domains of contiguous chromatin marked by an enrichment for interactions between loci within the domain as compared to loci in neighboring domains, termed topologically associating domains (TADs) [11]. Cohesin-dependent loop extrusion is counterbalanced by homotypic interactions within chromatin that drive the separation of the genome into euchromatic and heterochromatic compartments, referred to as A and B, via self-association [5,6]. It is believed that this tendency for chromatin to self-organize is driven by phase-separation of chromatin-associated proteins, especially within heterochromatin [12–15]. Genome folding changes upon differentiation [16,17], and specific loops are disrupted in disease [18], suggesting a functional role for genome architecture.

Higher order nuclear organization, in contrast, is created by the non-random location of genomic loci within the 3D space of the cell nucleus. A convenient indicator of 3D genome location is the radial position of a locus, denoting the degree of proximity to the nuclear lamina [19–21]. The nuclear lamina is a broadly repressive region marked by the presence of constitutive heterochromatic domains referred to as lamin-associated-domains (LADs) [22,23]. LADs are uniquely marked by characteristic chromatin modifications, in particular histone H3K9 dimethylation [24], which is likely recognized by proteins found at the lamina to target regions to peripheral positions. However, the specific proteins recognizing the mark are unknown, and radial positioning of different loci appears to require different factors [25]. Radial position in numerous examples correlates with gene activation, as many genes tend to move towards the nuclear interior from the periphery as they are transcriptionally activated, for instance immunoglobulins [26,27], Hox genes [28], and globin genes [29]. Furthermore, repositioning to the nuclear periphery often, but not always, silences genes [30–32], and radial position of specific genes is disrupted in cancer [33,34], suggesting a role for nuclear organization in gene regulation and cell fate.

It thus appears that both genome folding and nuclear organization have ramifications for genome function. Both genome folding and nuclear organization are also marked by high cell-to-cell variability [35]. Single-cell high-throughput chromosome conformation capture (Hi-C) and imaging-based studies have shown that pairwise interactions between any two genome loci generally only occur at low frequencies, and genome folding is marked by exceptional plasticity [36–39]. Furthermore, it is likely that even the most conserved and specific features, such as TADs, are dynamic structures representing the average of many different conformations [40–42]. Radial position similarly occurs in a probabilistic manner, such that any locus can be found at any position when examined in individual cells, and it is only in populations of cells that preferences arise [3,43]. LADs interact frequently with the lamina, by definition,

but also the edge of the nucleolus and can sometimes be found in the nucleoplasm itself [4]. Thus, while the principles of genome folding and nuclear organization are generally conserved, they are also both marked by extensive variability at the level of single cells and alleles.

Several models suggest that overall genome organization is informed by a combination of both genome folding and nuclear organization. Computational models suggest that self-association of heterochromatin, and its association with proteins at the nuclear lamina, are both required and sufficient to drive the separation of A and B compartments and their relative position within the nucleus [44]. Furthermore, integrative models of genome architecture involving both Hi-C (i.e. genome folding) and lamina-DamID (i.e. nuclear organization) data yield significant additional insights compared to models based on Hi-C or lamina-DamID data alone [45]. Similarly, a biochemical and sequencing-based approach, GPSeq, allows detection of distance to the nuclear lamina in populations of cells [46] and reveals functional diversity within the nucleus, with different loci, chromosomes, epigenetic states, and chromatin functions occurring in different radial positions. Models built with GPSeq data in combination with Hi-C data, rather than Hi-C data alone, better recapitulate real spatial positioning determined by DNA FISH [46]. However, as these computational models depend largely on separate datasets or measurements, and as biochemical or sequencing-based datasets largely rely on populations of cells, the relationship between chromatin folding and nuclear organization within a single nucleus is as yet unclear.

To address whether 3D nuclear position affects the frequency of a given chromatin interaction, we undertook a systematic analysis of both radial position and pairwise spatial distances at more than 100 locus pairs in human foreskin fibroblasts (HFF) and 25 locus pairs in human embryonic stem cells. We discovered that many chromatin interactions show preferred radial positions, and that loss of preferential positioning within the nucleus coincides with loss of enriched pairwise interaction frequencies. We also find that the likelihood that two loci colocalize in a given cell type can be altered by either cell-type-specific differences in mean distance or variability of distance. Our observations suggest that radial position within a nucleus and pairwise distance between two loci are correlated parameters that change in cell-type-specific ways, leaving open the possibilities that they are coregulated, for example by chromatin modification, or that altering one can drive changes in the other.

## Results

### Determination of radial position of chromatin-chromatin interactions

We set out to ask whether the likelihood of intrachromosomal chromatin interactions to occur is related to their radial position within the nucleus. To this end, we selected a set of 137 probe pairs among a total of 69 loci on human chromosomes 1, 4, 17, and 18 and located in the A as well as the B compartment (Fig 1A and S1 Table). Loci were selected to maximize the range of Hi-C capture frequencies at a given genomic distance, as described previously [37]. All probe pairs tested were between loci on the same chromosome and no inter-chromosomal interactions were analyzed due to their very low frequency [11]. Genomic distances between loci in tested interaction pairs ranged from ~52 kb to 235 Mb (Fig 1A and S2 Table). While detection efficiencies sometimes varied somewhat between probes or wells, we did not observe any differences in distance distributions or radial positions even considering wells with a wide range of detection efficiencies (S1B and S1C Fig). However, to eliminate possible minor effects of detection efficiency, only wells where at least 60% of cells showed an appropriate segmentation of two spots in each channel (consistent with an overall 77% detection efficiency in each channel) were considered. Furthermore, to ensure proper segmentation and assignment of minimum distances, only cells with two spots in each channel were considered. As a control for the

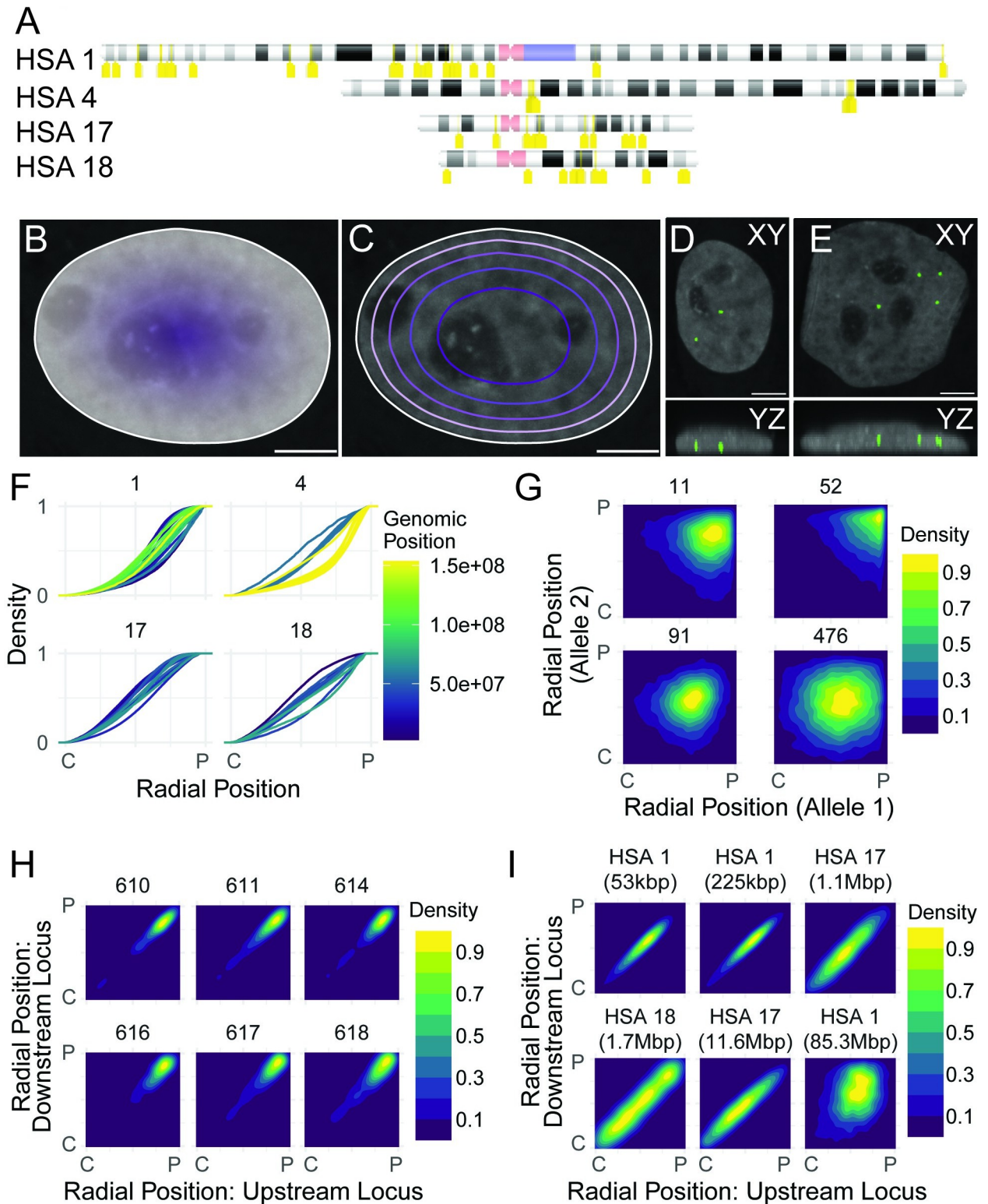


**Fig 1. Determination of radial position of genome regions.** A: Schematic location of genome probes used. Probes are indicated in yellow; centromeres in pink, pericentromeric regions in purple. B: Diagram of normalized Euclidean distance transform for continuous radial position, showing the calculation of a radial position for every position within the nucleus. Dark, central: 0. Light, peripheral: 1. Scale bar: 5  $\mu$ m. C: Diagram of equi-area concentric shell boundaries for one nucleus. Note that equi-area shells have square-root spacing relative to radial position itself. Scale bar: 5  $\mu$ m. D: Maximum projections in XY (top) and YZ (bottom) showing a cell with a “false central” spot that appears central in XY but is likely at

the very bottom of the cell in YZ. Scale bar: 5  $\mu\text{m}$ . E: Maximum projections in XY (top) and YZ (bottom) showing a cell with a “true central” spot which is central in XY as well as XZ. Scale bar: 5  $\mu\text{m}$ . F: CDFs showing continuous normalized radial position for all probes tested, separated into panels by chromosome. Position along chromosome is color-coded. G: Normalized 2D density plot for comparing radial positions at the two alleles in each cell of four example loci on chromosome 1, as marked in the figure. There is little to no observed correlation. Information about correlation coefficients and number of spots per locus is in [S1 Table](#). H: Normalized 2D density plots comparing radial position at probe 609 on chromosome 4 (x axis) and radial position at multiple adjacent target probes on chromosome 4 as specified (y-axis). Genomic distance between probe centers ranges from 0.25 Mbp (609–610) to 2.28 Mbp (609–618). I: Normalized 2D density plots comparing radial position at pairs of probes, with genomic distance between probes and chromosome as marked. Kbp: kilobasepairs. Mbp: megabasepairs. Probe pairs used (clockwise from top left): chr1 73.74, chr1 89.91, chr17 142.146, chr1 91.433, chr 17 40.86, and chr 18 186.193. For all panels, information about correlations and number of spot pairs per probe pair is in [S2 Table](#).

<https://doi.org/10.1371/journal.pgen.1010451.g001>

accuracy of distance measurements, a single locus was stained using all three fluorophores simultaneously, to experimentally determine the practical resolution of the microscope used. 95% of signals were within 187 nm, and the median distance was 91 nm with a standard deviation of 465 nm ([S1A Fig](#)). With the exception of the closest-spaced probe pair which was separated by 52 kb center-to-center, all interaction pairs showed higher separation distances. For example, probes separated by 224 kb had a median spatial distance of 180 nm and a standard deviation of 257 nm, statistically significantly different from our control pair (t-test:  $6 \times 10^{-4}$ ) ([S1A Fig](#)). This behavior confirmed that the resolution of the microscope and probes was sufficient to detect spatial separation between the locus pairs tested, as previously described [37]. For each interacting pair, we mapped the radial and Euclidean position of both interaction partners by DNA-FISH using BAC probes (see [Materials and Methods](#)). This dataset included a total of 932,261 analyzed spot pairs with a median of 3,333 spot pairs per probe pair ([S2 Table](#)).

FISH signals were identified using the Laplacian of the Gaussian method, which performed as well as previously used deep learning segmentation [47] ([S1B and S1C Fig](#)), and centers of gravity were determined for each spot in X and Y as this reduced noise in distance distributions ([S1D Fig](#), see [Materials and Methods](#)). The radial position for each probe signal was calculated based on the distance to the edge of the segmented cell nucleus in the DAPI channel, and normalized to the size of the nucleus such that 0 is fully central and 1 is fully peripheral ([Fig 1B](#)). Alternatively, the nuclear area was binned into concentric shells of equal area, and signals were assigned a radial shell according to their radial position ([Fig 1C](#)). Locus positions were determined in 2D projections as previously described [48] rather than in 3D reconstructions since the elongation of signals in the Z direction made it likely that a signal was visible in most Z positions within the nucleus and because the out-of-focus light and slight irregularities in the imaging well made it challenging to approximate the top or bottom of all the cells ([Fig 1D](#)). At the length scale used here, 2D analysis of projected images performed as well as 3D analysis for comparisons between two probe pairs or conditions, as previously reported [49]. Visual examination was occasionally used to confirm the localization of loci ([Fig 1D and 1E](#)).

### Radial positioning of genome loci is intrinsically variable

We first examined the population-level radial positioning of each tested probe using an empirical cumulative distribution function (ECDF; [Fig 1F](#)). As previously observed, different loci showed distinct localization preferences ([Fig 1F](#), all probes as histograms [S2 Fig](#); [43]). As entire chromosomes have characteristic radial positions, probes on the same chromosomes showed, as expected, similar distribution profiles, with the overall range of radial positioning preferences being somewhat smaller on chromosomes 17 and 18 than chromosomes 1 and 4 ([Fig 1F](#)). The two large regions on chromosome 4 with multiple loci tested per region showed different radial positioning patterns from each other but more consistent radial positioning across the contiguous genomic region ([Fig 1F](#), yellow lines vs blue lines).



We next asked whether the radial position of the two homologs in a nucleus are correlated to determine whether radial position varies intrinsically on the basis of the chromosome or extrinsically on the basis of the cell (Fig 1G). Analysis of 69 loci indicated that the radial position of the two homologs showed little correlation in individual cells (Figs 1G and S3A. Pearson and Spearman correlation coefficients for all loci included in S1 Table: range of Pearson correlation coefficients: -0.056 to 0.209; range of Spearman correlation coefficients: -0.053 to 0.226), in line with our previous observation that spatial distances between genomic loci were not correlated between homologs [37]. The position of loci varied independently within a preferred position, consistent with each individual chromosome's nuclear position being largely independent (Figs 1G and S3A). As expected, adjacent loci on a single chromosome often were strongly correlated at distances up to several million base pairs (Fig 1H and 1I), but loci spaced by extremely long distances (> 20 Mbp) often lost this correlation (Figs 1I and S4). These observations suggest that large regions within the genome, composed of multiple topological domains, move together relative to the nuclear periphery.

We next asked whether the measured radial position distributions correlated with LADs. For this assessment, we used publicly available DAM-ID sequencing data generated on the same fibroblast cell line [50,51]. We compared the radial position of all to the DAM-ID score (S3B Fig), as well as chromatin compartment assignments on the basis of Hi-C data [50,51]. We observed a general trend for the most-peripheral loci to be in LADs, and for peripheral loci to be more likely to be in LADs and B compartment heterochromatin than inter-LADs and A compartment euchromatin (S3B Fig). This trend was especially visible on chromosome 18, and somewhat apparent on chromosome 1, although inter-LAD loci were found at a very wide variety of radial positions (S3B Fig). We did not observe any correlation between LAD status or compartment and radial position on chromosomes 17 or 4 (S3B Fig). We also examined the enrichment of specific histone modifications (H3K4me3, H3K27ac) in published ChIP-seq datasets [52], and found no correlation between median or most common radial position and chromatin type as defined by either of these two metrics (S3B Fig). These findings are in line with the observation that LADs have been shown to not exclusively be localized to the nuclear periphery but also in the nuclear interior in individual cells [53].

### Colocalization between genome loci is enriched at specific radial positions

We next sought to determine whether proximity between two loci showed a preference for their radial location. To this end, we measured the spatial distance between interacting loci and at the same time determined the radial positions of each signal in the pair (Fig 2). With the exception of genomically proximal pairs on chromosome 4, most of these pairs colocalized rarely and the radial positions of the two loci were frequently quite different. As expected, the difference in radial positions between the two loci in the pair was strongly correlated with the spatial distance between the two loci (S5 Fig). However, more interesting was the fact that certain pairs showed a preference for pairwise colocalization at specific radial positions that was stronger than the preference of individual loci within the pair. We classified pairs of loci into three categories: 1) pairs which showed no dependence on radial position (Fig 2A, gray cell), 2) pairs which showed closer spatial proximity towards the center of the nucleus (Fig 2A, yellow cell), and 3) pairs which showed closer spatial proximity at the edge of the nucleus (Fig 2A, purple cell). We determined that comparing median spatial distances between radial bins could discriminate between these three patterns (Fig 2A, plot). As either locus of a pair of genome loci could show a preference for localization at a specific nuclear position, we separately compared spatial distances between the two loci to the radial position of each locus in the pair. Visual examination of 2D density plots of radial position of one spot in the pair versus

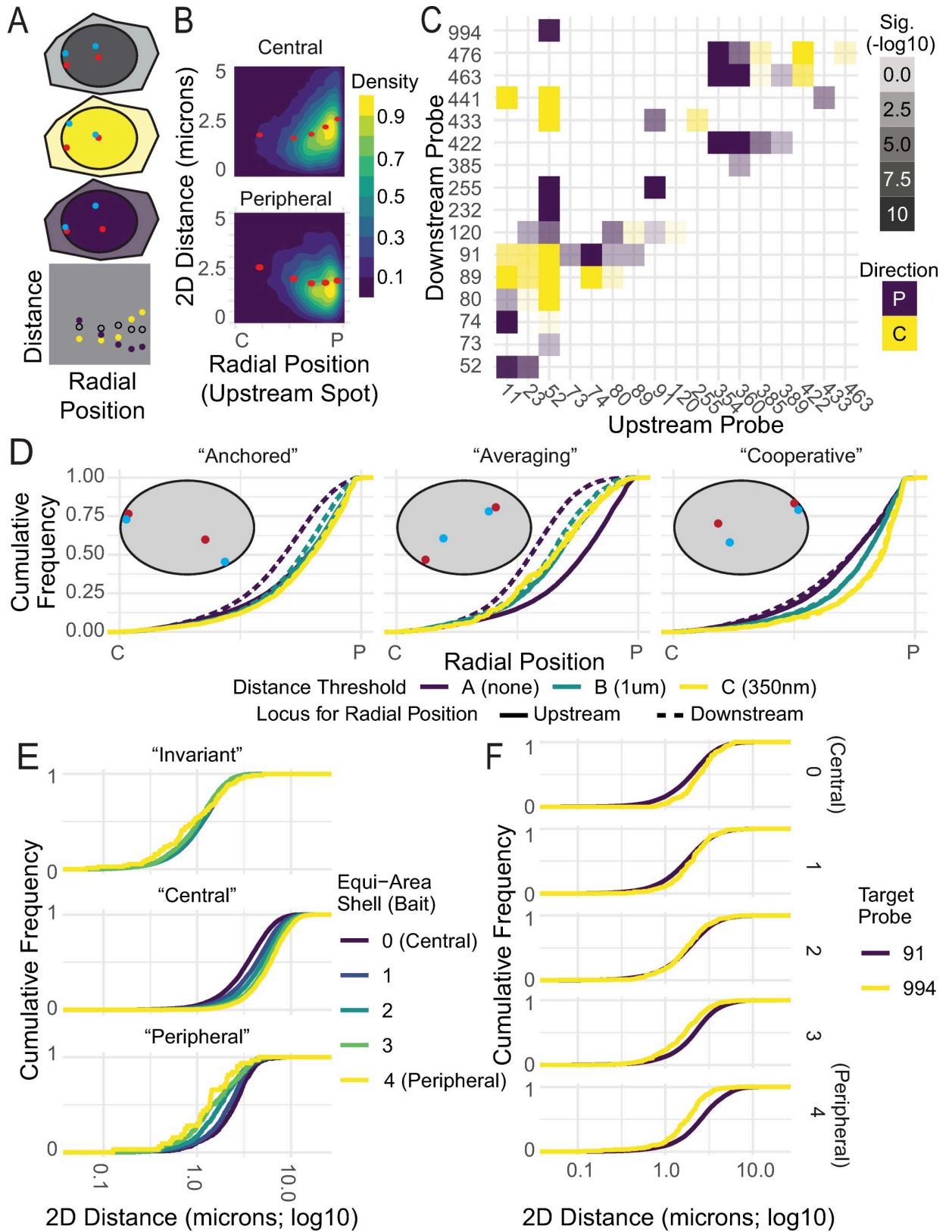


**Fig 2. Pairwise proximity shows preferred radial positions.** A: Schematic showing a pair without preference (transparent), more likely to interact at the center (future shown in yellow), edge (future shown in purple). In scatter plots they result in shifts in medians by bin as shown in

the bottom panel. B: Two examples of 2D density plots showing, respectively, a positive correlation between radial position and 2D spatial distance (i.e. interactions occur in the center of the nucleus) and a negative correlation between radial position and 2D spatial distance (i.e. interactions occur at the periphery). Correlation coefficients and number of spot pairs per probe pair is in [S2 Table](#). C: Heatmap showing overall correlation between radial position at the upstream locus and distance from the upstream to downstream locus for all pairs on chromosome 1 tested in HFFs. D: Examples of CDFs showing cumulative distributions of radial positions for both spots in pairs with various patterns of enrichment: one “Anchored” pair (chr1 11.52), one “Averaging” pair (chr1 52.89), and one “Cooperative” pair (chr1 52.255). 2D distance threshold between spots is shown in color (purple: farther apart than 1  $\mu\text{m}$ , teal: between 1  $\mu\text{m}$  and 350 nm, yellow: within 350 nm). Solid lines show the radial position of the upstream probe, dashed lines show the radial position of the downstream probe. Cartoons diagramming the behavior are included as an inset. E: CDFs showing 2D spatial distance on a log scale, color-coded by radial shell of the upstream probe in the pair. “Invariant” (chr17 86.123): no dependence between shell and spatial distance. “Central” (chr17 121.142): more central shells (shell 0) show shorter distances. “Peripheral” (chr1 91.255): more peripheral shells (shell 4) show shorter distances. F: CDFs showing position-dependent partner preference, with 2D distance to locus 52 on a log scale on the x-axis, comparing a peripherally-enriched partner (994, in yellow) to a centrally-enriched partner (91, in purple). Panels show radial shell of locus 52 (0 is most central, 4 is most peripheral).

<https://doi.org/10.1371/journal.pgen.1010451.g002>

spatial distance between spots revealed instances of each pattern ([Fig 2B](#)). Some locus pairs were more often found at shorter spatial distances near the center of the nucleus ([Fig 2B](#), top panel) whereas others were in closer proximity when near the periphery ([Fig 2B](#), bottom panel). These correlations were statistically significant when considered with an ANOVA test (Top panel: slope = 1.38,  $p = 4.93 \times 10^{-8}$ , Bottom panel: slope = -1.13,  $p = 1.41 \times 10^{-8}$ ).

To comprehensively analyze the relationship of colocalization frequency and radial position, we calculated four statistical parameters for each of the 137 interaction pairs: 1) the direction and 2) significance of correlation between radial position at the upstream probe and distance between the probes, and 3) the direction and 4) significance of correlation between radial position at the downstream probe and distance between the probes. To calculate significance, we used an ANOVA test to determine whether variance in radial position of either locus significantly contributed to variance in distance between the spots. To calculate direction, we used the slope of a least-squares linear regression model to determine whether shorter spatial distances were more common at peripheral or central locations. Instances where spot-to-spot distance depended on radial position were in fact common ([Figs 2C and S6](#)). Of the 137 pairs examined, 58% showed a significant correlation between spatial distance and radial position of at least one spot ( $p < 0.01$ ) and 22% showed a significant correlation between radial position of both spots ( $p < 0.01$ ). These correlations occurred at similar rates for enrichment at the edge of the nucleus or enrichment in the center of the nucleus. 45% of pairs were spatially closer together when one of the participating loci was at the edge of the nucleus, and 35% of pairs were closer together when one of the participating loci was in the center of the nucleus. Thus, a dependence on radial position is common, but not universal, and the degree and direction of enrichment appears to be specific to the locus pair. We conclude that the spatial distance between genome loci is often related to their 3D nuclear position.

Because the radial position of the two loci in the pair is not always exactly the same, we wanted to know if dependencies on radial position were more often caused by one locus in the pair moving towards the preferred radial position of another, or if they were driven by both loci in the pair moving together. We thus examined only those instances where both loci in a pair were found in the same radial shell, and determined how often in this filtered dataset there was a significant association between radial position of either spot and pairwise distance between the two spots ([S7 Fig](#)). We observed that association between radial position and spatial distance was more frequently significant when only pairs within the same radial shell were considered (76% of pairs showing a significant association with radial position of at least one spot, 74% of pairs showing a significant association with radial position of both spots). Most often, these pairs were more likely to be in spatial proximity at the edge of the nucleus (85% of associated pairs, or 65% of total pairs). This suggests that overall, when both loci are found at the edge of the nucleus, the spatial distance between them tends to be lower.



Nevertheless, in the entire dataset, there was a diversity of behaviors. The two loci in the pair were often in different radial shells (55% of the time). Furthermore, the 80 locus pairs that showed a correlation with location fell within three distinct groups with regard to their behavior (Fig 2D). First, for 36% of pairs a significant association between radial position and pairwise distance was only present when considering radial position of one of the two loci. We termed these “Anchored” since an ‘anchored’ spot was found at the same overall radial position irrespective of its distance to its ‘variable’ partner. In these cases, the ‘variable’ spot’s preferred radial position converged on this ‘anchored’ spot’s radial position as distance thresholds were decreased (Fig 2D). Second, 12% of pairs showed “Averaging” patterns, where the direction of the association was different between the two loci: close spatial proximity occurred when one locus was more central, and the other more peripheral (Fig 2D). Finally, 10% of pairs we termed “Cooperative”, as the radial position distributions for two loci were similar at all spatial distance thresholds, but colocalizing locus pairs occurred at different positions than pairs that were spatially farther apart (Fig 2D). It is worth noting that broad trends were visible between the types of pairs and their association patterns. “Averaging” pairs tended to occur between loci with disparate preferred radial positions, such as those between LADs and inter-LADs (9/16 pairs) or instances where one locus was most often peripheral and the other most often central (12/16 pairs). Similarly, “Cooperative” pairs tended to occur between two LADs or two interLADs (11/14 pairs) or between loci with similar radial positions (10/14 pairs).

The occurrence of significant, and pair-specific, associations between 2D spatial distance and radial position were confirmed by analysis of equi-area shells (Fig 2E). We observed some locus pairs with no significant dependence on radial position (top panel, Fig 2E), some pairs where shorter distances occurred in more central shells (middle panel, Fig 2E), and some pairs where shorter distances occurred in more peripheral shells (bottom panel, Fig 2E). We also observed that a locus can have different behaviors with different interacting partners. Thus, even for an individual locus pair, there is no universal rule determining proximity from the geometry of the nucleus, or chromatin density of a nuclear subcompartment. In fact, where a locus is within the nucleus in any individual cell can alter its spatial proximity to other loci. For example, probe 52 (chr1:12708720–12865743) tends to be spatially closer to locus 91 (10 Mbp away at chr1:22223363–22394657) when it is central and locus 994 (almost 250 Mbp away at chr1:248125294–248263553) when it is peripheral (Fig 2F). This tendency for one region to have different preferred partners at different radial positions suggests that repositioning a locus from one nuclear subcompartment to another may introduce that locus to a different chromatin environment, rather than pulling its most common interactors along with it (Fig 2F).

### Cell-type specificity and chromatin dependence of preferential colocalization sites

Chromatin properties differ between ES cells and differentiated cells. In particular, ESC chromatin is generally more homogeneously decondensed, contains very few heterochromatin domains and is hyperdynamic with regards to binding of chromatin proteins [54–56]. We took advantage of these differences in chromatin properties in HFFs and H1 human embryonic stem cells (hESCs) to ask whether the observed position dependence of colocalization is cell-type specific and affected by chromatin state. To do so, we selected a set of 26 locus pairs between 9 loci spanning approximately 30 Mbp on the p-arm of chromosome 1, which in HFFs show both “Cooperative” and “Averaging” patterns (Fig 3A, yellow tags). We comparatively mapped the spatial distance and radial position of these loci in H1 hESCs and HFFs (Fig 3).

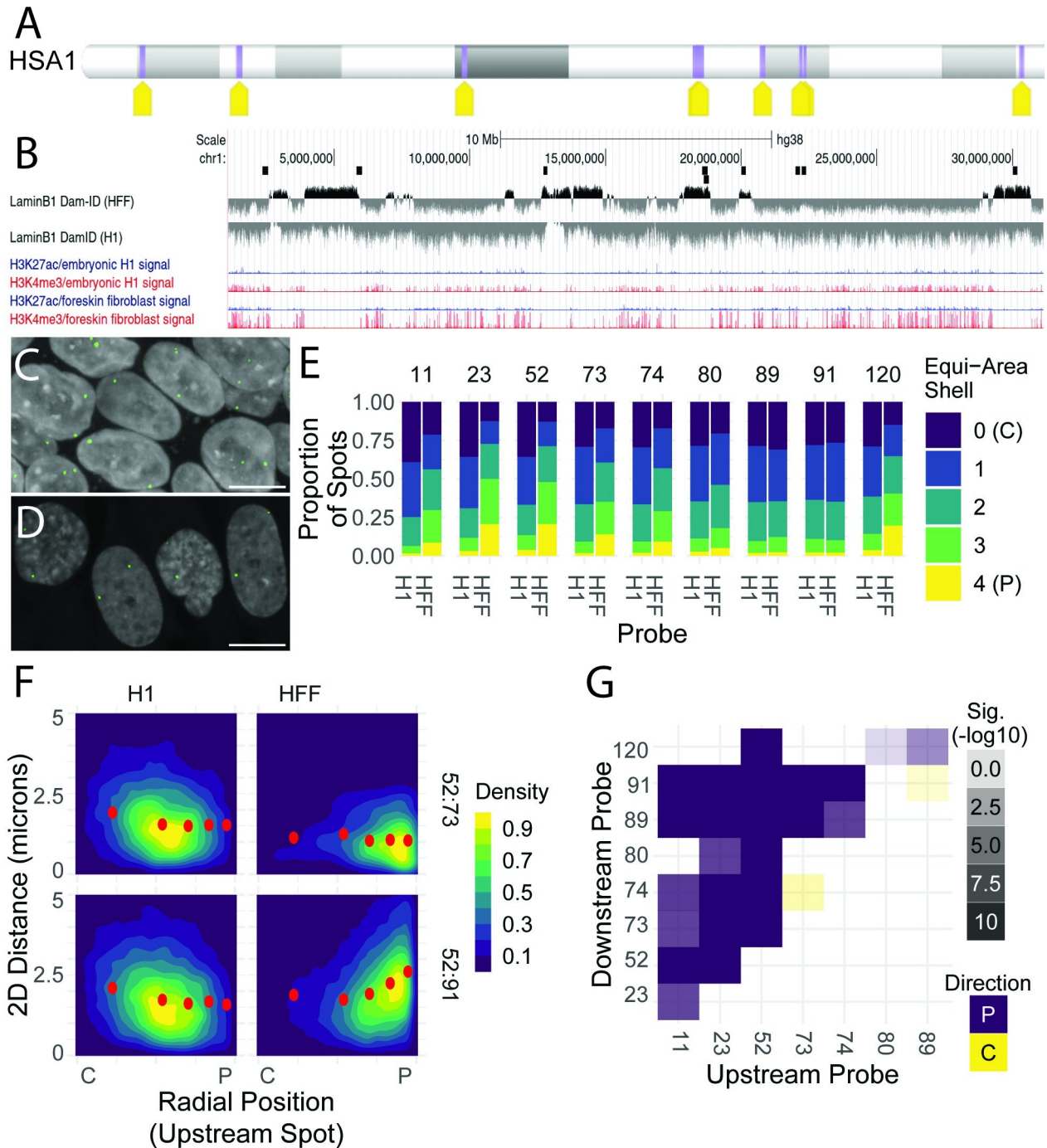


**Fig 3. Embryonic stem cells show centralization of probes but peripheral trend for interactions.** A: Schematic location of all probes tested in H1 embryonic cells on chromosome 1. Yellow tags: probes stained in H1 cells; purple bars: all probes stained in HFF cells. B: UCSC Genome Browser track showing LAD position and chromatin type for a region on the P arm of chromosome 1 in H1 hESCs (embryonic H1) and HFFs (foreskin fibroblast). C: Representative field of H1 human embryonic stem cells: DAPI staining (gray) and FISH (green). Scale bar: 10  $\mu$ m. D: Representative field of HFFs: DAPI staining (gray) and FISH (green). Scale bar: 10  $\mu$ m. E: Bar charts showing general centralization of all probes in this region in H1 cells relative to their position in HFF cells. F: 2D density plots showing radial position of one locus (locus 52) as a function of 2D spatial distance to a downstream locus (locus 73 or 91 as noted) in both HFFs and H1 hESCs. Correlation coefficients and number of spot pairs per locus pair is in [S2 Table](#). G: Heatmap showing correlation between radial position of upstream probe and pairwise spatial distance between two probes in H1 cells.

<https://doi.org/10.1371/journal.pgen.1010451.g003>

Publicly available sequencing data confirmed chromatin differences between these cell types at this region (Fig 3B). In HFFs, the chromosome 1 region contained seven large LADs and eight additional regions of positive Dam-ID signal that were too small to be classified as LADs (Fig 3B). In contrast, in H1 cells the same region was uniformly inter-LAD (Fig 3B). Somewhat surprisingly, the histone modification landscape of this region is less distinguishable between H1s and HFFs (Fig 3B). HFFs show regions of enrichment of H3K27 acetylation and especially H3K4 methylation in inter-LADs and depletion of these marks in LADs, and while the signal of both is overall lower in H1s, the same patterns arise (Fig 3B). This behavior suggests that while the LADs in this genome region are not stably associated with the periphery in H1 cells, the region has already begun to transition into heterochromatin and euchromatin.

We imaged and analyzed at least 500 H1 hESCs for each locus pair for a total of 153,204 analyzed pairs with a median of 4,572 signals per pair (S2 Table). In line with the more homogenous lamin B1 Dam-ID data in H1 cells, all loci tested were centrally located in H1 cells versus their frequently more peripheral localization in HFFs (Fig 3C and 3D; radial positions of all loci in both cell types S2 Fig). Complementary equi-area shell analysis revealed that while in HFFs many of the loci in this region are commonly found in peripheral shells 3 and 4, all loci tested in this region have a preference for central shells 0 and 1 in H1 cells (Fig 3E).

Similar to HFFs, in 2D density plots pairs of loci showed patterns of enrichments at certain radial positions in H1 cells (Fig 3F). Strikingly, while the overall centralization of all probes in H1 cells is visible in these graphs as an overall shift of density, the trend of association between radial position of one probe and spatial distance to a genomically distant probe was also in many cases different between H1 cells and HFF cells. In fact, in H1 cells all pairs showed the same trend: shorter spatial distances between pairs were slightly more common at peripheral positions, regardless of whether they were enriched at peripheral or central positions in HFFs (Fig 3F). We quantitated the relationship between location and spatial distance at every tested pair in H1 cells as we did in HFFs and confirmed this more consistent trend in H1 cells. While 58% (80/137) of pairs showed significant correlation between pairwise distance and radial position in HFF cells, 85% (22/26) of pairs showed significant correlation between distance and radial position in H1 cells (see Fig 3G for associations with radial position of upstream spot, S8A Fig for associations with radial position of downstream spot). This difference is significant by a hypergeometric test ( $p = 1.84 \times 10^{-3}$ ). Thus, in this region, more pairs show an association between radial position and spatial proximity in H1 cells than in HFFs, and that association is also more consistent in its direction, with colocalization more common at the periphery in H1 cells.

### Cell-type-specific enrichment of colocalization by decreased mean distance or increased variability

The fact that these loci were uniformly centrally located in stem cells and showed diverse preferred radial positions in fibroblasts is consistent with increased chromatin compartmentalization in fibroblasts driving relative enrichments and depletions in contact frequency, whereas the observed lack of heterochromatin blocks in stem cells [56] results in a more consistent and uniform dependence on genomic distance in this region. Examination of the chromosome 1 region in Hi-C maps from publicly-available micro-C data indeed confirms areas of enrichment and depletion of contact frequency in HFFs compared to H1s (Fig 4A). We calculated distance distributions from imaging data to determine the nature of cell-type specific differences in colocalization frequency and 2D distance. Overall, the range of average spatial distances was similar between HFFs and H1s. Median distances in both H1s and HFFs ranged from 1.1  $\mu\text{m}$  to 1.9  $\mu\text{m}$ , and as a population were not significantly different (Fig 4B; t-test

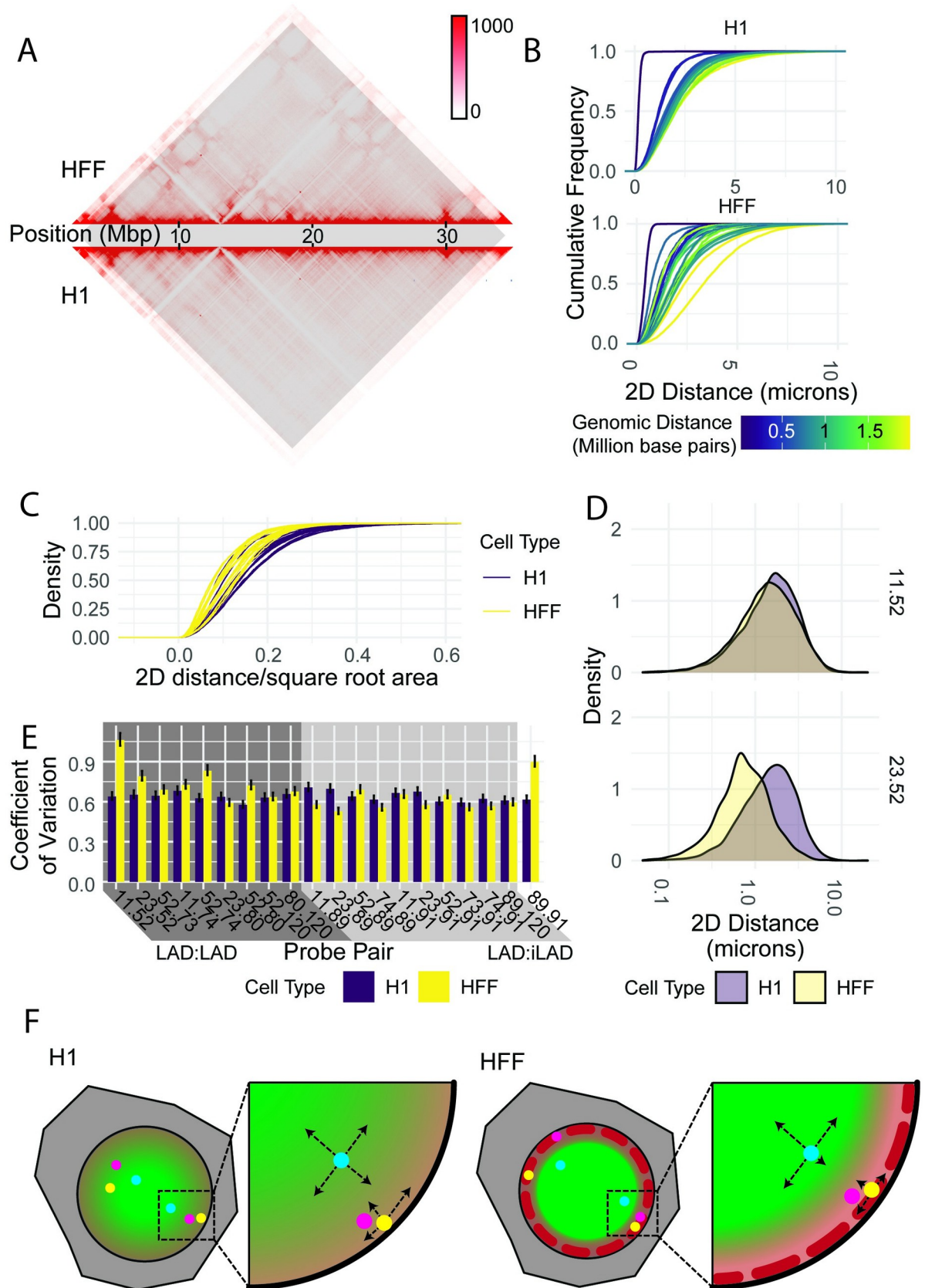




**Fig 4. Cell-type-specific pairwise associations have higher coefficients of variation.** A: Micro-C plots and compartment scores for studied region on the p-arm of chromosome 1 in HFF-c6 (top half) and H1 hESC (bottom half) cells. Region studied is highlighted. B: CDFs of 2D spatial distances between probes, color-coded by genomic distance, in H1 and HFF cells. C: CDFs of 2D spatial distances normalized to nuclear size (square root of area), color-coded by cell type. D: Representative PDFs showing 2D spatial distances between probes, color-coded by cell type, for two selected probe pairs (top panel: chr1 11.52; bottom panel: chr1 23.52). E: Bar graphs showing bootstrapped coefficient of variation in 2D spatial distance of a 1000-pair random subsample, sampled 1000 times, color-coded by cell type. Error bars: 95% confidence interval. F: Model cartoon showing suggested ways radial position can influence pairwise distance: in H1s largely geometric constraints mean the nuclear periphery acts as a barrier and closer proximities are more likely towards the edge of the nucleus. In HFFs, while this likely still plays a role, diverse chromatin environments further act to diversify genome architecture.

<https://doi.org/10.1371/journal.pgen.1010451.g004>

$p = 0.057$ ). After correction for the decreased nuclear size of H1 cells, 2D spatial distances were larger in H1 hESCs than in HFFs (Fig 4C; t-test  $p = 5.98 \times 10^{-4}$ ). This difference might be due to increased chromosomal intermingling in H1 hESCs versus HFFs, or it might be an artifact of the greater impact of projection on columnar H1 cells as versus relatively flat HFFs. This error was of particular concern as the 2-dimensional nature of this analysis would create a somewhat larger error in pairwise distances in columnar H1 hESCs than it does in flat HFFs, meaning that H1 distances overall may be more significantly under-estimated in this analysis. However, control experiments in morphologically similar cells suggest that the difference between 2D and 3D distances between probes in this region in stem cells were less than 5%, consistent with prior modelling (S8B Fig) [49]. This difference is of much smaller magnitude than the differences between median distances at specific probe pairs between HFF and H1 cells (Figs 4D and S8C), suggesting that the error yielded by differential bias due to projection was less than the real difference between cell types. A pronounced difference between the two cell types was, however, that in H1 cells, the 2D spatial distance distributions showed an almost perfect dependence on genomic distance, unlike in HFFs (Fig 4B;  $r^2$  0.94 in H1s, 0.41 in HFFs). Thus, while the total range of spatial distances may be independent of cell-type, and chromosomes in hESCs may occupy larger proportions of nuclear space, chromatin organization of this region in H1 cells appears to depend almost entirely on genomic distance, whereas in HFFs the distance between specific locus pairs often differs from the expected distance based on the genomic distance separating them. This is consistent with a model in which this region in H1 cells is organized as a globule within a single, mutually-interacting compartment, and the distance between two parts of the polymer is thereby mediated almost entirely by the length of polymer separating the two sites. This model fails in HFF cells, where distances are largely correlated with chromatin state and peripheralization as measured by lamin association (LAD status) suggesting a strong role of chromatin compartmentalization in determining spatial distances between loci. The fact that the changes in genomic-distance dependence and in radial position preference co-occur, despite chromatin compartments in H1 cells, suggests that segregation into LADs and inter-LADs with strongly preferred radial positions may contribute to the formation or stabilization of specific structures that bring certain regions close together and exclude others—or vice versa.

Cell-type-specific enriched colocalizations between pairs could either arise by a decrease in mean distance or, alternatively, via an increase in variability in spatial distance. This is because the proportion of a distance distribution within any given distance threshold will increase if the center of the distribution decreases, compressing the entire distribution closer to the threshold, or if the spread of the distribution increases, allowing a wider total range of distances. To discriminate between these two possibilities, we compared distance distributions of HFF-depleted (i.e. between LADs and inter-LADs in HFFs) and HFF-enriched (i.e. between two LADs in HFFs) locus pairs. Statistically significant changes in mean distance and variability were very common in these loci. 6 of 9 HFF-enriched pairs showed a statistically significant decrease in mean distance (t-test,  $p < 0.05$  after Bonferroni correction), and 6 of 10 HFF-



depleted pairs showed a statistically significant increase in mean distance (t-test,  $p < 0.05$ ). Similarly, 4 of 9 HFF-enriched and 5 of 10 HFF-depleted pairs showed a statistically significant change in variability (asymptotic test for equality of coefficients of variation,  $p < 0.05$ ).

When comparing changes in mean distance and variability of individual pairs, we find that one HFF-enriched pair and two HFF-depleted pairs showed altered variability but not altered distance. Colocalization between probe 11 (chr1: 2370451–2570719) and probe 52 (chr1: 12708718–1286743), separated by approximately 10 Mbp, is more likely to occur in HFFs than in stem cells (5.2% vs 4.0% within 350 nm; 0.5% vs. 0.2% within 100 nm;  $p < 0.005$  by a two-sample proportion test). However, the mean spatial distance between the two cell types is very similar (Fig 4D; 1.80  $\mu\text{m}$  in fibroblasts vs 1.85  $\mu\text{m}$  in stem cells,  $p = 0.0183$  by a t-test). This is made up for by an increase in variability (Fig 4D; standard deviation 1.58 in fibroblasts and 1.22 in stem cells,  $p = 9.23 \times 10^{-34}$  by the asymptotic test).

Similarly, in five of nine HFF-enriched pairs and five of ten HFF-depleted pairs, changes in mean distance alone, without a significant change in variability, were sufficient to drive enrichments. This is the case for colocalization between probe 23 (chr1: 5829955–6030168) and probe 52 (chr1: 12708718–1286743), separated by about 7 Mbp. Colocalizations within 350 nm or 100 nm were substantially more common in HFFs than in stem cells (13% vs. 3.8%,  $p < 2.2 \times 10^{-16}$  for 350 nm; 0.89% vs 0.27% for 100 nm,  $p < 0.0005$  by a two-sample proportion test). The mean distance between probes was substantially shorter in HFFs than in H1s (Fig 4D; 0.73  $\mu\text{m}$  in fibroblasts vs 1.52  $\mu\text{m}$  in stem cells;  $p = 9.42 \times 10^{-71}$  by a t-test), but HFFs exhibited a lower standard deviation (0.81 for HFFs vs 1.17 for stem cells).

While these results point to distinct behavior of individual locus pairs, it is worth noting that in both examples, the end result is an increased coefficient of variation that was statistically significant ( $p < 1 \times 10^{-4}$  in both cases by the asymptotic test). In fact, this trend for an increased coefficient of variation of spatial distance at HFF-enriched locus pairs in HFFs was the most consistent feature of HFF-enriched pairs (Fig 4F). To verify the reproducibility of this, in a way unbiased by the sample size, we performed a bootstrapping analysis to calculate the coefficient of variation for each probe pair in 1000 subsamples of 1000 spot pairs each. In every case where a pair colocalized more frequently in HFFs, the coefficient of variation in HFFs was also higher; in half of them it was statistically significant ( $p < 0.05$  after multiple hypothesis testing, see [Materials and Methods](#)) (Fig 4E). In the case of pairs that colocalized less frequently in HFFs, the differences in coefficient of variation were more mixed; while many were statistically significant after correction, some pairs showed higher variability in H1 cells and others showed higher variability in HFF cells (Fig 4E). This behavior is consistent with a model for long-range heterochromatin organization whereby both restricting the spatial distance or increasing the mobility of loci can alter colocalization frequency, the first by reducing the mean of the distance distribution and the second by increasing the spread.

Our analysis in H1 cells not only shows that genome structure at this region in H1s is overall more uniformly dependent on genomic distance than in HFFs, but also that the deviations from expected contact frequencies based on genomic distance that we observe in HFFs may be driven either by changes in average distance or changes in variability of distance (Fig 4F).

## Discussion

Genome mapping methods have found that both the position of a locus relative to the edge of the nucleus and the position of a locus relative to other loci are non-random [1]. Despite the emergence of non-random patterns, genome organization is also characterized by extensive single-cell variability. Chromosome positioning, and radial positioning of specific genes, has long been characterized as probabilistic rather than deterministic [57] and spatial distances

between genomic sites are marked by considerable intrinsic variability [35,37]. However, studies comparing the effect of the nuclear position of genomic loci and their proximity to distal loci in individual nuclei have been lacking. Here we used high-throughput imaging to simultaneously determine the radial coordinates and spatial distance for 137 chromatin interaction pairs between 69 loci on four chromosomes in HFF cells and 26 pairs between 9 loci on chromosome 1 in H1 human embryonic stem cells to ask whether the position of loci within the nucleus affects their proximity. We find that the position within the nucleus is associated with differential spatial distances, and that loss of preferred localization within the nucleus is related to decreased rates of enriched interactions as well as decreased variabilities.

Most of the locus pairs we tested showed some dependence between nuclear position and colocalization frequency, suggesting an interrelation between genome folding and nuclear organization. It might be tempting to hypothesize either that the nuclear periphery of differentiated cells, with its overall increased chromatin density and geometric constraints may force genomically distant regions closer together, or that the nuclear center, with its generally open and accessible chromatin and lower potential maximum distance between loci, may allow colocalizations especially at long distances. However, what we observe is that preferences exist for increased proximity at the center of the nucleus and at the periphery of the nucleus, and that these preferences are highly specific to the cell type and locus pair studied. In embryonic stem cells, the region we tested was broadly euchromatic and centrally located, and yet every tested locus pair was more likely to be spatially closer together when at the edge of the nucleus. In fibroblasts, we observed many different pairs with many different patterns, but the preference for increased spatial proximity at the nuclear periphery is also apparent when considering locus pairs with both loci in the same radial shell in HFFs. These observations suggest that the nuclear periphery facilitates spatial proximity between genomically distant loci.

A simple explanation for this observation is that the periphery is characterized by increased chromatin density, which would shorten all local distances. Two observations argue against this interpretation. First, the density and segregation of peripheral heterochromatin increases during differentiation [58], and the periphery in stem cells is marked by lower levels of A-type lamins and heterochromatic marks [59,60], so the expectation would be that a chromatin-density-mediated effect would be stronger in HFF cells than H1 hESCs, which is contrary to what we observe. Second, a chromatin density effect would be more prevalent at short-range associations, which reliably move together into the denser environment of the nuclear periphery. In contrast to this prediction, we find trends for short-range as well as long-range associations, and the strongest trends in fibroblasts are for long-range associations between loci whose radial positions correlate only poorly. Instead, it seems more likely that the observed preference for peripheral localization of interactions in embryonic stem cells is largely due to geometric effects, whereby short-range movements of two loci brought together early in G1, when higher order genome organization is established, cannot move loci far apart at the edge as easily as they can in the center. In fact, slower movement of loci tethered to the nuclear periphery has been observed [61]. The relative immobility of the interaction partners may increase their likelihood of spatial proximity throughout the rest of the cell cycle. In this model, the same geometric constraints—and the tethering of regions to the nuclear lamina—act to reduce the ‘search volume’ for particular long-range interactions, thus increasing their rates of interaction as we observe in fibroblasts (Fig 4F).

We find that the correlations between nuclear organization and genome folding are generally stronger in fibroblasts compared to hESCs, and that the directionality of these correlations is more variable in fibroblasts than in hESCs. These trends coincide with differences in chromatin structure between fibroblasts and hESCs, pointing to a role of nuclear subcompartmentalization in chromatin folding. Stem cells have a unique, generally more open and globally

permissive chromatin environment with overall increased levels of euchromatic marks [55] and reactivation of otherwise stably silenced transposable elements [62]. Significant and global rearrangements of the heterochromatin compartment occur during differentiation [58]. In line with these properties, we find that in stem cells there is a consistent effect of location on most locus pairs, whereas in fibroblasts we observe pair-specific effects, suggesting that the trend for specific pairs to interact at specific locations within the nucleus may depend on their chromatin type. In stem cells, which do not show differential nuclear organization at the loci analyzed, preferential pairing between loci is also lost. Furthermore, even within fibroblasts, we observed that enriched interactions between LADs tended to occur, perhaps unsurprisingly, at the edge of the nucleus, and that in the relatively rare instances where normally peripheral loci were found in the center of the nucleus, they were more likely to be in spatial proximity to genome loci with which they rarely interacted in the overall population. Thus, it seems reasonable to conclude that a strongly heterotypic chromatin landscape arising during differentiation allows the segregation of frequent interacting pairs, but flexibility in nuclear organization as observed in stem cells allows loci to sample the entire range of nuclear positions and interacting partners, thus maintaining plasticity.

Based on the higher level of compartmentalization and higher degree of heterochromatin in fibroblasts, one might expect that fibroblast-enriched pairing events would show decreased variability in their separation distance. In contrast we find increased variability of highly interacting loci in fibroblasts. We observe increases in colocalizations concomitant with decreased mean distance without a change in variation and with increased variation without a change in mean distance. While there are many systems in which enrichment in colocalization frequency does not correlate with mean distance [63], our observations are among the first to directly show that increased variability in distance can lead to enrichment of colocalizations. This behavior could be due to increased local mobility of the loci, enabling them to scan a larger 3D space for potential partners, for instance when enhancer elements become more mobile upon activation [64]. Alternatively, it could be because in a differentiated nucleus which contains more distinct subcompartments, such as heterochromatin, the motion of loci is more constrained driving increased proximity if the two interaction partners are within the same compartment and decreasing proximity if they are located in distinct compartments, and thereby increasing variability. It is tempting to hypothesize that chromatin segregation, in addition to separating heterochromatin and euchromatin, may also alter variability and plasticity in chromatin folding.

There are three technical caveats to our study. First, our use of 2D rather than 3D measurements. second, the relatively small size of the probe sets relative to the genome, and third, the fact that our work is correlative rather than mechanistic. We do not believe that any of these limitations invalidates our findings. 2D measurements on projected images were used for practical reasons so as to reduce computation time and increase throughput. Prior analysis demonstrated very limited loss of accuracy of distance measurements on the length scales analyzed here [49]. In addition, errors introduced by 2D approximations would cause us to underestimate the rates of true peripheral localizations and thus make it more difficult to detect correlations between spatial distance and nuclear position as we have found here. The correlation we observed between LAD status or chromatin marks and radial positioning was indeed not strong and might be strengthened by segmenting nuclei in 3D. Similarly, for pairs where we did not see a dependence between radial position and pairwise distance, we cannot rule out the possibility that with 3D positions such a dependence would be detected. While it is therefore possible that we missed some dependencies that truly exist in 3D data, it is not likely that the dependencies we observed are not present. Furthermore, although our probe set is limited, the loci cover a wide range of chromatin features including location in diverse chromatin

environment, short- and long-range interactions and locations in gene dense and gene poor genome regions. More comprehensive analysis should be possible using whole-genome-imaging techniques [65]. Finally, the differences we observe between H1 hESCs and HFFs are correlations, and proper mechanistic studies of isogenic cells—such as altering the structure of the nuclear periphery using genetic techniques in differentiated cells, or specifically targeting individual model loci to different nuclear compartments and examining the effects on pairwise distances—are required to flesh out the true mechanisms driving the differential organization observed here.

Taken together, our results uncover an interdependence of chromatin interactions and radial positions in the cell nucleus. Our findings point to a close interplay of local chromatin folding and higher order nuclear organization and they highlight the need of using a multi-parametric and, ultimately, a multi-omics approach to studying nuclear architecture.

## Materials and methods

### HFF culture

HFFs were grown and plated for imaging exactly as described previously [37].

### H1 ESC cell culture

H1 human embryonic stem cells were grown on Matrigel (Corning #354277) in complete mTeSR media (StemCell Technologies). They were split every five days or when colonies began to merge, at a ratio of 1:10–1:12 depending on density. Matrigel was aliquoted into portions equivalent to  $\frac{1}{4}$  the lot-specified dilution factor, sufficient to dilute into 6.25 mL for plating all wells in a 6-well plate. Matrigel plates were made fresh at each split: one aliquot of Matrigel was diluted with 6.25 mL DMEM-F12 on ice, and 1 mL diluted Matrigel was added to each well of an ice-cold 6-well dish. The dish was rotated and shaken to make sure the entire surface of the dish was covered with Matrigel, and allowed to solidify at room temperature for at least 30 min. The supernatant was then removed and replaced with 2 mL room temperature mTeSR media. To split, cells were first washed with PBS and then treated with 1 mL ReLeSR cell dissociation reagent. The majority of the dissociation reagent was gently aspirated from the cells and they were placed in a humid incubator for 6 min. After this incubation, fresh mTeSR media was placed in the well and colonies were lifted by vigorously tapping the dish for 45 sec. The resulting cell suspension was pipetted once through a 1 mL serological pipette to break down colonies and transfer them into a 15 mL conical tube for passaging. The well was then washed with an additional 1 mL mTeSR media, and an appropriate amount of cell suspension was added to each well of the prepared plate (200  $\mu$ L for a 1:10 split). The plate was shaken to spread cells evenly before being returned to the incubator. Between splits, media was replaced with 2 mL fresh room temperature complete mTeSR each day.

For FISH experiments, 384-well plates were coated with Matrigel exactly as described above, with a volume of 25  $\mu$ L diluted Matrigel per well of a 384-well plate. To plate as colonies, 800  $\mu$ L suspended colonies were diluted 1:10 with 7.2 mL mTeSR, and 50  $\mu$ L of this diluted cell suspension was added to each well of the prepared 384 well dish. Cells were grown as colonies for three days before fixation.

To plate as a single cell suspension, cells were rinsed once with PBS and incubated in 1 mL ReLeSR/well of a 6-well at 37°C for 8 min. Cells were lifted and dissociated by pipetting with a 1 mL micropipette three times and added to a tube containing 1 mL DMEM/F-12 to neutralize the ReLeSR. Wells were washed with 1 mL fresh DMEM/F-12 for a total of 3 mL cell suspension per well. Cells were then pelleted by spinning for 5 min at 300 x g at room temperature, and media was replaced with 5 mL complete mTeSR media supplemented with 1X ReVitaCell

ROCK Inhibitor (Thermo Fisher). Cells were gently, but completely, resuspended by tapping the tube as media was being added and subsequently pipetted twice with a 1 mL micropipette. 100  $\mu$ L cell suspension was plated per well of a 384-well plate, and cells were spun for 1 min at 300  $\times$  g at room temperature to settle and spread. Monolayer cells were grown overnight and fixed the next day. Experimental results were comparable in both cases and as such data were pooled between dispersed and colony-grown measurements.

## DNA FISH

DNA FISH was done as described [66].

## Imaging

Imaging of HFFs was done as described [66].

H1 colonies were imaged in an automated fashion on a Yokogawa CV7000 microscope. To automatically find H1 colonies, we used Wako's SearchFirst platform (Wako Software Suite). Each well in the plate was initially imaged in the blue channel (Ex: 405 nm, Em: 445/45 nm) at 4x magnification. Colonies were segmented in these images using KNIME, and a uniform tiled grid of all positions in the well within colonies was determined. Of these, 20 positions were chosen at random to image in four colors at 60X. Imaging proceeded as for HFFs on the Yokogawa CV7000 microscope, with the exception of the height of the z-stack, which was increased to 15  $\mu$ m in order to capture the entire nucleus.

## Computational analysis

Image processing, including nuclear segmentation, spot segmentation, calculation of the center of gravity in three dimensions and radial position were performed in Python using this Jupyter Notebook (<https://github.com/elfinn/cell-and-spot-segmentation>). In brief, images were maximally projected prior to segmentation of nuclei using CellPose, a deep-learning based model for segmentation of nuclei including those which touch or have slight overlaps in the 2D maximum projection [67]. Centers of gravity in Z were calculated at this step for each pixel in the image where possible. Individual nuclei were cropped in each channel and radial positions for each pixel within each nucleus were pre-calculated using an exact Euclidean distance transform and normalized such that fully central pixels had radial position 0 and edge-pixels had radial position 1. Nuclei were also binned into five concentric shells of equal area, and spots were assigned to whichever shell their central pixel fell. Within each nucleus, spots were identified using the Laplacian of the Gaussian, which while not quite as sensitive at segmenting spots as a previously trained neural network (S1B Fig, [47]) nonetheless resulted in accurate, and in fact indistinguishable, distance distributions (S1C Fig).

We determined Cartesian coordinates for all spots as centers of gravity as previously applied to localizations of small probes [68], which resulted in a reduction of noise in the distance distributions and a shift in median distance for positive colocalization controls (same probe stained with two colors) from 323 nm to 111 nm (S1D Fig). For each spot, we recorded radial position at the pixel-level spot center and center of gravity calculated in X, Y, and Z where possible for the region defined by half maximum signal normalized to cellular background around each spot center. Subsequent pairwise distances were calculated and statistical analyses performed in R, as described below.

To select cells in which FISH staining and segmentation had proceeded robustly, we considered only those cells which met all the following criteria: 1) At least two spots in each relevant channel, 2) the same number of spots in each relevant channel, 3) coming from a well in which at least 60% of nuclei have exactly two spots segmented. All pairwise distances between



spots in different colors were calculated, and minimum distances on a per-green-spot basis (or per-red-spot in the case of comparisons between red and far-red probes) were selected. This final dataset included a list of all spots considered, with X, Y, and radial coordinates (a total of approximately 1,643,000 spots), as well as a list of all minimum pairwise distances along with X, Y, and radial coordinates for both spots in the pair (a total of approximately 1,116,000 pairs).

To map probed loci to previously published sequencing data: We used Lamin-B1 Dam-ID-seq data and Compartment scores generated from Micro-C data in the HFF-c6 and H1 cell lines from the 4D Nucleome consortium [50,51] (accession numbers:

4DNESZJMHC3O and 4DNESKOBVYIY respectively for micro-C and

4DNESXZ4FW4T and 4DNESXKBPZKQ respectively for LaminB1-DamID-seq) as well as ChIP-seq data from ENCODE [52,69] (ENCSR814XPE and ENCSR000ANP for H3K4me3 and H3K27ac respectively in H1 hESCs, and ENCSR639PCR and ENCSR510VXV for H3K4me3 and H3K27ac respectively in HFF-c6 cells). In each case, datasets were cross-referenced with our probe sets using the UCSC table browser (<https://genome.ucsc.edu/cgi-bin/hgTables>). In cases where a BAC probe overlapped multiple annotated features in the dataset, the median score was used. Genomic distances between pairs of loci were calculated from center to center, and distance to the nearest annotated LAD was calculated from edge to edge.

To ensure homogeneity in the sample size across all locus pairs tested, which was essential for some analyses such as ANOVA tests, we performed random subsampling with replacement to generate a uniform dataset with 1000 spot pairs per locus pair. When a graph or test was done on subsampled, rather than raw, data, it is indicated in the text. Graphs were generated using ggplot2 [70].

R markdown files to calculate spot distances, perform subsequent analyses, and generate figures are available at <https://github.com/elfinn/radpos-r-code>.

## Supporting information

**S1 Fig. Validation of imaging pipeline.** A: Box and jitter plots showing distribution of distances for a selection of probe pairs including a costained control locus (Distance 0) as well as several probe pairs at genomic distances up to ~16 Mbp. Center-to-center genomic distance is color-coded. B: Comparative spots per cell for spots segmented from three representative wells with a deep-learning based published model [47] as compared to and traditional Laplacian of Gaussian-based segmentation. Wells selected for a breadth of FISH quality, from very high signal to noise (well 5) to borderline (well 8). C: Spot-to-spot distance distributions calculated from the spots segmented in (B). Color-coded by pair of channels within the well. D: Spot-to-spot distances for the 120:120 costained locus with spot positions assigned by center of gravity (top) or central pixel (bottom). (TIF)

**S2 Fig. Histograms for radial position.** Histograms showing radial position of all spots at all loci in both cell types. Legend for each panel is: cell type (top line), chromosome and probe number (bottom line; chr.probe). For radial position, a value of 0 is fully central and a value of 1 is fully peripheral. (TIF)

**S3 Fig. Intrinsic variability in radial position at all tested loci and correlations with sequencing data.** A: Normalized 2D Density plots showing radial position at one homolog (arbitrarily selected) on the x-axis and radial position at the other homolog on the y-axis. Probe and chromosome as marked. B: Scatterplots showing median continuous normalized

radial position vs. sequencing metrics: LaminB1 enrichment by Dam-ID, Chromatin Compartment in Micro-C, H3K27me3 and H3K4me3 signal in ChIP-seq. Color-coded by most common radial shell.

(TIF)

**S4 Fig. Correlation between radial positions at all probes tested.** 2D Density plots showing radial position at one locus in a pair on the x-axis and the other locus on the y-axis. Probe pair and chromosome as marked.

(TIF)

**S5 Fig. Correlation between difference in radial positions and spatial distance.** 2D Density plots showing difference in radial position between loci in a pair on the x-axis and spatial distance between loci the y-axis. Probe pair and chromosome as marked.

(TIF)

**S6 Fig. Heatmaps for direction and significance of dependence on radial position for all pairs in HFF cells.** Heatmaps for each pairwise interaction on a chromosome, with probe number (approximate genomic position) on both x and y axis. Intensity of color (alpha) is significance (as  $-\log_{10}(\text{p-value})$  in the ANOVA test). Color is direction (as slope of line of best fit).

(TIF)

**S7 Fig. Heatmaps for direction and significance of dependence on radial position for pairs in the same radial shell HFF cells.** Heatmaps for each pairwise interaction on a chromosome, considering only those instances where both loci in the pair are found within the same radial shell. Probe number (approximate genomic position) is on both x and y axis. Intensity of color (alpha) is significance (as  $-\log_{10}(\text{p-value})$  in the ANOVA test). Color is direction (as slope of line of best fit).

(TIF)

**S8 Fig. Supplemental information for H1 data.** A: Heatmap showing association between radial position of downstream spot and spatial distance between spots, for each pairwise interaction on a chromosome, with probe number (approximate genomic position) on both x and y axis. Intensity of color (alpha) is significance (as  $-\log_{10}(\text{p-value})$  in the ANOVA test). Color is direction (as slope of line of best fit). B: Median ratio between 2D and 3D distances for 14 pairs of loci on chromosome 1 in columnar stem cells. Error bars are median absolute deviation in 3D/2D ratio. C: Probability density functions showing 2D spatial distance distribution for all pairs examined in both HFFs and H1s. Pair is as marked, color-coding by cell type.

(TIF)

**S1 Table. Locus positions and HFF data.** Coordinates: genome coordinates in the format chrX:Start-End. Chr: chromosome. Start: start position of BAC probe. End: end position of BAC probe. Probe: internal probe ID for purposes of figures. Cell\_Type: Cell type for radial position data. Count: number of spots analyzed. LaminB1: Normalized Lamin-B1 Dam-ID signal in HFFs. Compartment: Compartment score from micro-C in HFFs. H3K27me3: H3K27me3 ChIP-seq signal in HFFs. H3K36me3: H3K36me3 ChIP-seq signal in HFFs. H3K4me3: H3K4me3 ChIP-seq signal in HFFs. LAD dist: end-to-end distance to nearest LAD in HFFs. Median R: median radial position. Mean R: mean radial position. Mode R: most common equi-area radial shell. Pearson: Pearson Correlation Coefficient (PCC) for correlation between radial position at one homolog and radial position at the other homolog. Spearman: Spearman correlation coefficient (SCC) for correlation between radial position at one homolog

and radial position at the other homolog.  
(CSV)

**S2 Table. Pairwise distance summary statistics.** Chr: chromosome. Probe1: Upstream internal probe ID. Probe2: Downstream internal probe ID. Region: probeset that probe pair belong to. Cell\_Type: Cell type. Count: Number of spot pairs analyzed. 100nm: Number of spot pairs within 100 nm. 350nm: Number of spot pairs within 350 nm. 1um: Number of spot pairs within 1 micron. Median: Median distance between spots. SD: standard deviation in distance between spots. Mean: mean distance between spots. CoV: Coefficient of variation in distance between spots. Pearson\_spotvspot: PCC for correlation between radial position at upstream spot and radial position at downstream spot. Spearman\_spotvspot: SCC for correlation between radial position at upstream spot and radial position at downstream spot. Pearson\_r1vdist: PCC for correlation between radial position at upstream spot and distance between spots. Spearman\_r1vdist: SCC for correlation between radial position at upstream spot and distance between spots. Pearson\_r2vdist: PCC for correlation between radial position at downstream spot and distance between spots. Spearman\_r2vdist: SCC for correlation between radial position at downstream spot and distance between spots. Slope\_r1vdist: slope of linear model between radial position at upstream spot and distance between spots. Slope\_r2vdist: slope of linear model between radial position at downstream spot and distance between spots. ANOVA\_r1vdist: p-value of ANOVA test comparing spatial distance between spots by radial bin of upstream spot. ANOVA\_r2vdist: p-value of ANOVA test comparing spatial distance between spots by radial bin of downstream spot.  
(CSV)

## Author Contributions

**Conceptualization:** Elizabeth H. Finn, Tom Misteli.

**Data curation:** Elizabeth H. Finn.

**Formal analysis:** Elizabeth H. Finn.

**Funding acquisition:** Tom Misteli.

**Methodology:** Elizabeth H. Finn.

**Project administration:** Tom Misteli.

**Supervision:** Tom Misteli.

**Visualization:** Elizabeth H. Finn.

**Writing – original draft:** Elizabeth H. Finn, Tom Misteli.

**Writing – review & editing:** Elizabeth H. Finn, Tom Misteli.

## References

1. Misteli T. The Self-Organizing Genome: Principles of Genome Architecture and Function. *Cell*. 2020; 183(1):28–45. <https://doi.org/10.1016/j.cell.2020.09.014> PMID: 32976797
2. Rowley MJ, Corces VG. Organizational principles of 3D genome architecture. *Nat Rev Genet*. 2018; 19(12):789–800. <https://doi.org/10.1038/s41576-018-0060-8> PMID: 30367165
3. Crosetto N, Bienko M. Radial Organization in the Mammalian Nucleus. *Frontiers in genetics*. 2020; 11:33. <https://doi.org/10.3389/fgene.2020.00033> PMID: 32117447
4. van Steensel B, Belmont AS. Lamina-Associated Domains: Links with Chromosome Architecture, Heterochromatin, and Gene Repression. *Cell*. 2017; 169(5):780–91. <https://doi.org/10.1016/j.cell.2017.04.022> PMID: 28525751

5. Nuebler J, Fudenberg G, Imakaev M, Abdennur N, Mirny LA. Chromatin organization by an interplay of loop extrusion and compartmental segregation. *Proc Natl Acad Sci U S A*. 2018; 115(29):E6697–E706. <https://doi.org/10.1073/pnas.1717730115> PMID: 29967174
6. Schwarzer W, Abdennur N, Goloborodko A, Pekowska A, Fudenberg G, Loe-Mie Y, et al. Two independent modes of chromatin organization revealed by cohesin removal. *Nature*. 2017; 551(7678):51–6. <https://doi.org/10.1038/nature24281> PMID: 29094699
7. Hansen AS, Pustova I, Cattoglio C, Tjian R, Darzacq X. CTCF and cohesin regulate chromatin loop stability with distinct dynamics. *Elife*. 2017;6. <https://doi.org/10.7554/eLife.25776> PMID: 28467304
8. Busslinger GA, Stocsits RR, van der Lelij P, Axelsson E, Tedeschi A, Galjart N, et al. Cohesin is positioned in mammalian genomes by transcription, CTCF and Wapl. *Nature*. 2017; 544(7651):503–7. <https://doi.org/10.1038/nature22063> PMID: 28424523
9. Haarhuis JHI, van der Weide RH, Blomen VA, Yáñez-Cuna JO, Amendola M, van Ruiten MS, et al. The Cohesin Release Factor WAPL Restricts Chromatin Loop Extension. *Cell*. 2017; 169(4):693–707.e14. <https://doi.org/10.1016/j.cell.2017.04.013> PMID: 28475897
10. Wutz G, Várnai C, Nagasaka K, Cisneros DA, Stocsits RR, Tang W, et al. Topologically associating domains and chromatin loops depend on cohesin and are regulated by CTCF, WAPL, and PDS5 proteins. *EMBO J*. 2017; 36(24):3573–99. <https://doi.org/10.15252/embj.201798004> PMID: 29217591
11. Lieberman-Aiden E, Berkum NLV, Williams L, Imakaev M, Ragoczy T, Telling A, et al. Comprehensive Mapping of Long-Range Interactions Reveals Folding Principles of the Human Genome. *Science*. 2009; 326(5950):289–93. <https://doi.org/10.1126/science.1181369> PMID: 19815776
12. Larson AG, Elnatan D, Keenen MM, Trnka MJ, Johnston JB, Burlingame AL, et al. Liquid droplet formation by HP1 $\alpha$  suggests a role for phase separation in heterochromatin. *Nature*. 2017; 547(7662):236–40. <https://doi.org/10.1038/nature22822> PMID: 28636604
13. Sabari BR, Dall'Agnese A, Boija A, Klein IA, Coffey EL, Shrinivas K, et al. Coactivator condensation at super-enhancers links phase separation and gene control. *Science*. 2018; 361(6400). <https://doi.org/10.1126/science.aar3958> PMID: 29930091
14. Shin Y, Chang Y-C, Lee DSW, Berry J, Sanders DW, Ronceray P, et al. Liquid Nuclear Condensates Mechanically Sense and Restructure the Genome. *Cell*. 2018; 175(6):1481–91.e13. <https://doi.org/10.1016/j.cell.2018.10.057> PMID: 30500535
15. Strom AR, Emelyanov AV, Mir M, Fyodorov DV, Darzacq X, Karpen GH. Phase separation drives heterochromatin domain formation. *Nature*. 2017; 547(7662):241–5. <https://doi.org/10.1038/nature22989> PMID: 28636597
16. Bonev B, Mendelson Cohen N, Szabo Q, Fritsch L, Papadopoulos GL, Lubling Y, et al. Multiscale 3D Genome Rewiring during Mouse Neural Development. *Cell*. 2017; 171(3):557–72.e24. <https://doi.org/10.1016/j.cell.2017.09.043> PMID: 29053968
17. Dixon JR, Jung I, Selvaraj S, Shen Y, Antosiewicz-Bourget JE, Lee AY, et al. Chromatin architecture reorganization during stem cell differentiation. *Nature*. 2015; 518(7539):331–6. <https://doi.org/10.1038/nature14222> PMID: 25693564
18. Lupiáñez DG, Kraft K, Heinrich V, Krawitz P, Brancati F, Klopocki E, et al. Disruptions of Topological Chromatin Domains Cause Pathogenic Rewiring of Gene-Enhancer Interactions. *Cell*. 2015; 161(5):1012–25. <https://doi.org/10.1016/j.cell.2015.04.004> PMID: 25959774
19. Cremer T, Cremer C. Chromosome territories, nuclear architecture and gene regulation in mammalian cells. *Nat Rev Genet*. 2001;2. <https://doi.org/10.1038/35066075> PMID: 11283701
20. Manuelidis L, Borden J. Reproducible compartmentalization of individual chromosome domains in human CNS cells revealed by in situ hybridization and three-dimensional reconstruction. *Chromosoma*. 1988; 96(6):397–410. <https://doi.org/10.1007/BF00303033> PMID: 3219911
21. Manuelidis L. Individual interphase chromosome domains revealed by in situ hybridization. *Hum Genet*. 1985;71.
22. Hoskins VE, Smith K, Reddy KL. The shifting shape of genomes: dynamics of heterochromatin interactions at the nuclear lamina. *Current opinion in genetics & development*. 2021; 67:163–73. <https://doi.org/10.1016/j.gde.2021.02.003> PMID: 33774266
23. Pickersgill H, Kalverda B, de Wit E, Talhout W, Fornerod M, van Steensel B. Characterization of the *Drosophila melanogaster* genome at the nuclear lamina. *Nat Genet*. 2006; 38(9):1005–14. <https://doi.org/10.1038/ng1852> PMID: 16878134
24. Poleshko A, Smith CL, Nguyen SC, Sivaramakrishnan P, Wong KG, Murray JI, et al. H3K9me2 orchestrates inheritance of spatial positioning of peripheral heterochromatin through mitosis. *Elife*. 2019;8. <https://doi.org/10.7554/eLife.49278> PMID: 31573510

25. Shachar S, Voss TC, Pegoraro G, Sciascia N, Misteli T. Identification of Gene Positioning Factors Using High-Throughput Imaging Mapping. *Cell*. 2015; 162(4):911–23. <https://doi.org/10.1016/j.cell.2015.07.035> PMID: 26276637
26. Kosak ST, Skok JA, Medina KL, Riblet R, Le Beau MM, Fisher AG, et al. Subnuclear compartmentalization of immunoglobulin loci during lymphocyte development. *Science*. 2002;296. <https://doi.org/10.1126/science.1068768> PMID: 11935030
27. Zhou J, Ermakova OV, Riblet R, Birshtein BK, Schildkraut CL. Replication and subnuclear location dynamics of the immunoglobulin heavy-chain locus in B-lineage cells. *Mol Cell Biol*. 2002; 22(13):4876–89. <https://doi.org/10.1128/MCB.22.13.4876-4889.2002> PMID: 12052893
28. Lanctôt C, Kaspar C, Cremer T. Positioning of the mouse Hox gene clusters in the nuclei of developing embryos and differentiating embryoid bodies. *Exp Cell Res*. 2007; 313(7):1449–59. <https://doi.org/10.1016/j.yexcr.2007.01.027> PMID: 17346703
29. Francastel C, Magis W, Groudine M. Nuclear relocation of a transactivator subunit precedes target gene activation. *Proc Natl Acad Sci U S A*. 2001; 98(21):12120–5. <https://doi.org/10.1073/pnas.211444898> PMID: 11593025
30. Finlan LE, Sproul D, Thomson I, Boyle S, Kerr E, Perry P, et al. Recruitment to the nuclear periphery can alter expression of genes in human cells. *PLoS Genet*. 2008; 4(3):e1000039. <https://doi.org/10.1371/journal.pgen.1000039> PMID: 18369458
31. Reddy KL, Zullo JM, Bertolino E, Singh H. Transcriptional repression mediated by repositioning of genes to the nuclear lamina. *Nature*. 2008; 452(7184):243–7. <https://doi.org/10.1038/nature06727> PMID: 18272965
32. Kumaran RI, Spector DL. A genetic locus targeted to the nuclear periphery in living cells maintains its transcriptional competence. *The Journal of cell biology*. 2008; 180(1):51–65. <https://doi.org/10.1083/jcb.200706060> PMID: 18195101
33. Leshner M, Devine M, Roloff GW, True LD, Misteli T, Meaburn KJ. Locus-specific gene repositioning in prostate cancer. *Mol Biol Cell*. 2016; 27(2):236–46. <https://doi.org/10.1091/mbc.E15-05-0280> PMID: 26564800
34. Meaburn KJ, Agunloye O, Devine M, Leshner M, Roloff GW, True LD, et al. Tissue-of-origin-specific gene repositioning in breast and prostate cancer. *Histochem Cell Biol*. 2016; 145(4):433–46. <https://doi.org/10.1007/s00418-015-1401-8> PMID: 26791532
35. Finn EH, Misteli T. Molecular basis and biological function of variability in spatial genome organization. *Science*. 2019; 365(6457):eaaw9498. <https://doi.org/10.1126/science.aaw9498> PMID: 31488662
36. Nagano T, Lubling Y, Stevens TJ, Schoenfelder S, Yaffe E, Dean W, et al. Single-cell Hi-C reveals cell-to-cell variability in chromosome structure. *Nature*. 2013; 502(7469):59–64. <https://doi.org/10.1038/nature12593> PMID: 24067610
37. Finn EH, Pegoraro G, Brandão HB, Valton A-L, Oomen ME, Dekker J, et al. Extensive Heterogeneity and Intrinsic Variation in Spatial Genome Organization. *Cell*. 2019; 176(6):1502–15.e10. <https://doi.org/10.1016/j.cell.2019.01.020> PMID: 30799036
38. Cattoni DI, Cardozo Gizzi AM, Georgieva M, Di Stefano M, Valeri A, Chamousset D, et al. Single-cell absolute contact probability detection reveals chromosomes are organized by multiple low-frequency yet specific interactions. *Nat Commun*. 2017; 8(1):1753. <https://doi.org/10.1038/s41467-017-01962-x> PMID: 29170434
39. Bintu B, Mateo LJ, Su J-H, Sinnott-Armstrong NA, Parker M, Kinrot S, et al. Super-resolution chromatin tracing reveals domains and cooperative interactions in single cells. *Science*. 2018; 362(6413). <https://doi.org/10.1126/science.aau1783> PMID: 30361340
40. Hansen AS, Cattoglio C, Darzacq X, Tjian R. Recent evidence that TADs and chromatin loops are dynamic structures. *Nucleus*. 2018; 9(1):20–32. <https://doi.org/10.1080/19491034.2017.1389365> PMID: 29077530
41. Gabriele M, Brandão HB, Grosse-Holz S, Jha A, Dailey GM, Cattoglio C, et al. Dynamics of CTCF and cohesin mediated chromatin looping revealed by live-cell imaging. *Science*. 2022; 376(6592):496–501. <https://doi.org/10.1126/science.abn6583> PMID: 35420890
42. Shi G, Liu L, Hyeon C, Thirumalai D. Interphase human chromosome exhibits out of equilibrium glassy dynamics. *Nat Commun*. 2018; 9(1):3161. <https://doi.org/10.1038/s41467-018-05606-6> PMID: 30089831
43. Takizawa T, Meaburn KJ, Misteli T. The meaning of gene positioning. *Cell*. 2008; 135(1):9–13. <https://doi.org/10.1016/j.cell.2008.09.026> PMID: 18854147
44. Falk M, Feodorova Y, Naumova N, Imakaev M, Lajoie BR, Leonhardt H, et al. Heterochromatin drives compartmentalization of inverted and conventional nuclei. *Nature*. 2019; 570(7761):395–9. <https://doi.org/10.1038/s41586-019-1275-3> PMID: 31168090



45. Li Q, Tjong H, Li X, Gong K, Zhou XJ, Chiolo I, et al. The three-dimensional genome organization of *Drosophila melanogaster* through data integration. *Genome biology*. 2017; 18(1):145. <https://doi.org/10.1186/s13059-017-1264-5> PMID: 28760140
46. Girelli G, Custodio J, Kallas T, Agostini F, Wernersson E, Spanjaard B, et al. GPSeq reveals the radial organization of chromatin in the cell nucleus. *Nature biotechnology*. 2020; 38(10):1184–93. <https://doi.org/10.1038/s41587-020-0519-y> PMID: 32451505
47. Gudla P, Nakayama K, Pegoraro G, Misteli T. SpotLearn: Convolutional Neural Network for Detection of Fluorescence In Situ Hybridization (FISH) Signals in High-Throughput Imaging Approaches. *Cold Spring Harbor Symposia on Quantitative Biology*. 2017; 82:033761.
48. Shachar S, Pegoraro G, Misteli T. HIPMap: A High-Throughput Imaging Method for Mapping Spatial Gene Positions. *Cold Spring Harb Symp Quant Biol*. 2015;2015/10/17. <https://doi.org/10.1101/sqb.2015.80.027417> PMID: 26472748
49. Finn EH, Pegoraro G, Shachar S, Misteli T. Comparative analysis of 2D and 3D distance measurements to study spatial genome organization. *Methods*. 2017;2017/02/10. <https://doi.org/10.1016/j.jmeth.2017.01.007> PMID: 28179124
50. Dekker J, Belmont AS, Guttman M, Leshyk VO, Lis JT, Lomvardas S, et al. The 4D nucleome project. *Nature*. 2017; 549(7671):219–26. <https://doi.org/10.1038/nature23884> PMID: 28905911
51. Reiff SB, Schroeder AJ, Kirli K, Cosolo A, Bakker C, Mercado L, et al. The 4D Nucleome Data Portal: a resource for searching and visualizing curated nucleomics data. *bioRxiv*. 2021:2021.10.14.464435.
52. An integrated encyclopedia of DNA elements in the human genome. *Nature*. 2012; 489(7414):57–74. <https://doi.org/10.1038/nature11247> PMID: 22955616
53. Kind J, Pagie L, Ortobozkoyun H, Boyle S, de Vries Sandra S, Janssen H, et al. Single-Cell Dynamics of Genome-Nuclear Lamina Interactions. *Cell*. 2013; 153(1):178–92. <https://doi.org/10.1016/j.cell.2013.02.028> PMID: 23523135
54. Hinde E, Cardarelli F, Chen A, Khine M, Gratton E. Tracking the mechanical dynamics of human embryonic stem cell chromatin. *Epigenetics & Chromatin*. 2012; 5(1):20. <https://doi.org/10.1186/1756-8935-5-20> PMID: 23259580
55. Harikumar A, Meshorer E. Chromatin remodeling and bivalent histone modifications in embryonic stem cells. *EMBO Rep*. 2015; 16(12):1609–19. <https://doi.org/10.15252/embr.201541011> PMID: 26553936
56. Meshorer E, Misteli T. Chromatin in pluripotent embryonic stem cells and differentiation. *Nature reviews Molecular cell biology*. 2006; 7(7):540–6. <https://doi.org/10.1038/nrm1938> PMID: 16723974
57. Sehgal N, Fritz AJ, Vecerova J, Ding H, Chen Z, Stojkovic B, et al. Large-scale probabilistic 3D organization of human chromosome territories. *Human molecular genetics*. 2016; 25(3):419–36. <https://doi.org/10.1093/hmg/ddv479> PMID: 26604142
58. Politz JC, Scalzo D, Groudine M. Something silent this way forms: the functional organization of the repressive nuclear compartment. *Annual review of cell and developmental biology*. 2013; 29:241–70. <https://doi.org/10.1146/annurev-cellbio-101512-122317> PMID: 23834025
59. Rober RA, Weber K, Osborn M. Differential timing of nuclear lamin A/C expression in the various organs of the mouse embryo and the young animal: a developmental study. *Development*. 1989; 105(2):365–78. <https://doi.org/10.1242/dev.105.2.365> PMID: 2680424
60. Constantinescu D, Gray HL, Sammak PJ, Schatten GP, Csoka AB. Lamin A/C Expression Is a Marker of Mouse and Human Embryonic Stem Cell Differentiation. *Stem Cells*. 2006; 24(1):177–85. <https://doi.org/10.1634/stemcells.2004-0159> PMID: 16179429
61. Chubb JR, Boyle S, Perry P, Bickmore WA. Chromatin motion is constrained by association with nuclear compartments in human cells. *Curr Biol*. 2002; 12(6):439–45. [https://doi.org/10.1016/s0960-9822\(02\)00695-4](https://doi.org/10.1016/s0960-9822(02)00695-4) PMID: 11909528
62. Grow EJ, Flynn RA, Chavez SL, Bayless NL, Wossidlo M, Wesche DJ, et al. Intrinsic retroviral reactivation in human preimplantation embryos and pluripotent cells. *Nature*. 2015; 522(7555):221–5. <https://doi.org/10.1038/nature14308> PMID: 25896322
63. Fudenberg G, Imakaev M. FISH-ing for captured contacts: towards reconciling FISH and 3C. *Nat Methods*. 2017;2017/06/13. <https://doi.org/10.1038/nmeth.4329> PMID: 28604723
64. Gu B, Swigut T, Spencley A, Bauer MR, Chung M, Meyer T, et al. Transcription-coupled changes in nuclear mobility of mammalian cis-regulatory elements. *Science*. 2018; 359(6379):1050–5. <https://doi.org/10.1126/science.aao3136> PMID: 29371426
65. Nguyen HQ, Chatteraj S, Castillo D, Nguyen SC, Nir G, Lioutas A, et al. 3D mapping and accelerated super-resolution imaging of the human genome using in situ sequencing. *Nat Methods*. 2020; 17(8):822–32. <https://doi.org/10.1038/s41592-020-0890-0> PMID: 32719531
66. Finn EH, Misteli T. A high-throughput DNA FISH protocol to visualize genome regions in human cells. *STAR protocols*. 2021; 2(3):100741. <https://doi.org/10.1016/j.xpro.2021.100741> PMID: 34458868

67. Stringer C, Wang T, Michaelos M, Pachitariu M. Cellpose: a generalist algorithm for cellular segmentation. *Nature Methods*. 2021; 18(1):100–6. <https://doi.org/10.1038/s41592-020-01018-x> PMID: [33318659](https://pubmed.ncbi.nlm.nih.gov/33318659/)
68. Mateo LJ, Murphy SE, Hafner A, Cincini IS, Walker CA, Boettiger AN. Visualizing DNA folding and RNA in embryos at single-cell resolution. *Nature*. 2019; 568(7750):49–54. <https://doi.org/10.1038/s41586-019-1035-4> PMID: [30886393](https://pubmed.ncbi.nlm.nih.gov/30886393/)
69. Davis CA, Hitz BC, Sloan CA, Chan ET, Davidson JM, Gabdank I, et al. The Encyclopedia of DNA elements (ENCODE): data portal update. *Nucleic acids research*. 2018; 46(D1):D794–d801. <https://doi.org/10.1093/nar/gkx1081> PMID: [29126249](https://pubmed.ncbi.nlm.nih.gov/29126249/)
70. Wickham H. *ggplot2: Elegant Graphics for Data Analysis*. New York: Springer-Verlag; 2009 2009.